Journal of Materials Chemistry C

Accepted Manuscript

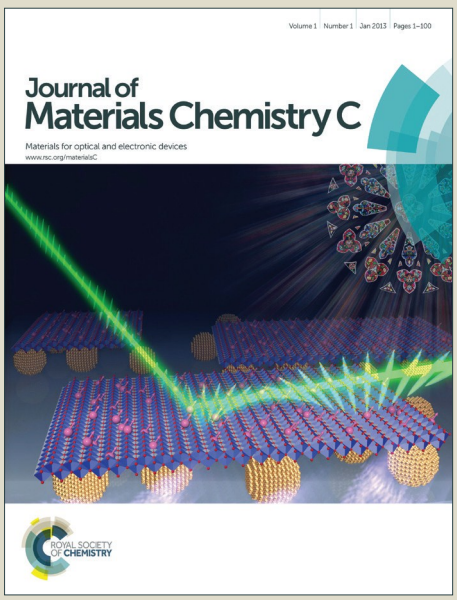

ROYAL SOCIETY OF CHEMISTRY

www.rsc.org/materialsC

Solution-derived $YBa_2Cu_3O_7$ superconducting films with $BaZrO_3$ nanodots based on reverse micelle stabilized nanoparticles

Iñigo Bretos,[‡a] Theodor Schneller,*[a] Martina Falter,[b] Michael Bäcker,[b] Eugen Hollmann,[c] Roger Wördenweber,[c] Leopoldo Molina-Luna,[d,e] Gustaaf Van Tendeloo[e] and Oliver Eibl[f]

[a]*Institut für Werkstoffe der Elektrotechnik II, RWTH Aachen, D-52074 Aachen, Germany*
[b]*Deutsche Nanoschicht GmbH, D-53359 Rheinbach, Germany*
[c]*Peter Grünberg Institut (PGI-8), Forschungszentrum Jülich GmbH, D-52425 Jülich, Germany*
[d]*Technische Universität Darmstadt, Department of Material- and Geosciences, Alarich-Weiss-Strasse 2, 64287 Darmstadt, Germany*
[e]*EMAT, University of Antwerp, Groenenborgerlaan 171, 2020 Antwerp, Belgium*
[f]*Institut für Angewandte Physik, Universität Tübingen, D-72074 Tübingen, Germany*

Superconducting $YBa_2Cu_3O_{7-\delta}$ (YBCO) films with artificial $BaZrO_3$ (BZO) nanodots were prepared by a chemical solution deposition method involving hybrid solutions comprised of trifluoroacetate-based YBCO precursors and reverse micelle stabilized BZO nanoparticle dispersions. Microemulsion-mediated synthesis was used to obtain nano-sized (~12 nm) and mono-dispersed BZO nanoparticles that preserve their features once introduced into the YBCO solution, as revealed by dynamic light scattering. Phase pure, epitaxial YBCO films with randomly oriented BZO nanodots distributed over their whole microstructure were grown from the hybrid solutions on (100) $LaAlO_3$ substrates. The morphology of the YBCO/BZO nanocomposite films was strongly influenced by the amount of nanoparticles incorporated to the system, with contents ranging from 5 to 40 mol%. Scanning electron microscopy showed a high density of isolated second-phase defects consisting of BZO nanodots in the nanocomposite film with 10 mol% of BZO. Furthermore, a direct observation and quantitative analysis of lattice defects in the form of interfacial edge dislocations directly induced by the BZO nanodots was evidenced by transmission electron microscopy. The superconducting properties (77 K) of the YBCO films improved considerably by the presence of such nanodots, which seem to enhance the morphology of the sample and therefore the intergranular critical properties. The incorporation of preformed second-phase defects (here, BZO) during the growth of the superconducting phase is the main innovation of this novel approach for the all-solution based low-cost fabrication of long-length coated conductors.

‡ I.B. is now at Instituto de Ciencia de Materiales de Madrid (ICMM-CSIC), E-28049 Madrid, Spain.
* To whom correspondence should be addressed. E-mail: schneller@iwe.rwth-aachen.de. Phone: (+49) 241 80 27820. Fax: (+49) 241 80 22300.

Introduction

The increasing energy demand and depletion of fossil fuels as well as the global warming require the development of energy efficient technologies for power conversion and distribution of electrical power. High-temperature superconductors (HTS) are destined to revolutionize the electrical engineering in the coming years based on their superior power performance (two orders of magnitude higher than conventional copper wires) and affordable costs of the liquid nitrogen working fluid (two orders of magnitude lower than 4 K cryogenics).[1] Second-generation (2G) HTS wires, or coated conductors, have emerged as a significant alternative to commercial Ag-sheathed PIT (powder-in-tube) tapes of $Bi_2Sr_2Ca_2Cu_2O_x$ belonging to the first generation (1G).[2-4] They basically consist of an epitaxial superconducting layer, generally $YBa_2Cu_3O_{7-\delta}$ (YBCO), grown on a flexible substrate with several textured buffer layers displaying higher critical current densities J_c, lower processing costs, and better electrical performance at higher temperatures and magnetic fields with respect to the preceding 1G technology (see Figure 1). Therefore, there is a fast-growing worldwide interest in 2G HTS wires for applications such as underground transmission cables, high-efficiency motors, compact generators and high field magnets.[5-7]

The fabrication of coated conductors is usually carried out by physical methods involving vacuum deposition [e.g., sputtering, pulsed laser deposition (PLD)]. Epitaxy is achieved either via buffer layers obtained by ion-beam assisted deposition (IBAD) or inclined substrate deposition (ISD), or rolling-assisted biaxial texturing of the substrate (RABiTS).[8] During the last years, chemical solution deposition (CSD)[9] has revealed as a reliable method for the preparation of long-length coated conductors focusing not only on

the superconducting YBCO film, but even extending to the buffer layers that complete their architecture.[10-15] Since it is a non-vacuum method, less expensive equipment is required, what joined to the flexibility in composition variations and the potential to coat large area substrates make the technique[16] optimum for the development of an *all-solution* based process of fabrication.[17-19,] Superconducting films with large critical currents are obtained when a high epitaxial level and densification is achieved,[20] i.e., avoiding a large misalignment between the YBCO grains that would locally reduce the critical current density. For power applications, strong pinning of magnetic flux lines is required as well.[21] This can be done either by naturally formed defects (vacancies, dislocations, twin boundaries) or by artificial pinning centers systematically introduced in the films.[22] The lower density of the formers usually prevents a complete confinement of vortices at relatively high magnetic fields.[23,24] Effectiveness in pinning mechanism is enhanced by the incorporation of additional nanoscale inhomogeneities into the superconducting matrix through different engineering strategies.[25] Heavy-ion irradiation was initially employed to produce columnar defects in YBCO single crystals consisting in aligned and discontinuous tracks of damaged material.[26] The J_c values were observed to increase and a strong directionality of the pinning force was found. On the other hand, high densities of second-phase defects (YBa_2CuO_5 nanodots) were obtained by growth of alternating multilayers of $YBa_2Cu_3O_7$ and YBa_2CuO_5 using PLD, with in-field critical currents at 77 K increased by a factor of two.[27] Addition of rare earth (RE) elements also provided significant enhancement of pinning in the corresponding films based on the segregation of precipitates from the YBCO phase [e.g., $RE_2Cu_2O_5$, $(Y,RE)_2O_3$].[28-30] Similar to this approach, the formation of nanoparticles non-inherent to the YBCO

system (e.g.; $BaZrO_3$, $BaIrO_3$, $CaZrO_3$) showed larger enhancements of J_c and excellent retention of this value under high magnetic fields in films prepared by PLD.[31 - 33] Presently, one of the most efficient vortice-pinning mechanism for coated conductors consists in the preparation of YBCO/$BaZrO_3$ nanocomposite films by CSD,[34] making the technique not only effective but also economically feasible. The uniform distribution and random orientation (common features found by solution methods) of the $BaZrO_3$ nanoscale defect structures within the YBCO epitaxial matrix provides a unique microstructure responsible for the strong and isotropic flux pinning obtained.[35]

The present report describes the preparation of $YBa_2Cu_3O_{7-\delta}$ superconducting films with artificial $BaZrO_3$ (hereinafter, BZO) defects via another chemical solution deposition technique. The introduction of the BZO nanodots is carried out by a novel method based on the addition of various amounts of reverse micelle stabilized BZO nanoparticle dispersions into trifluoracetate-based (TFA) YBCO precursor solutions to form nanocrystalline extrusions within the superconductor matrix. Microemulsion-mediated synthesis is used to obtain the BZO nanoparticle dispersions, which allows a precise control over the final size and distribution of the particles in the medium.[36,37] It is generally known that magnetic flux lines in a superconductor mainly depends on the size, density and geometry of the corresponding defects.[38,39] The nano-sized and ideally non-agglomerated powders of BZO present in the dispersions of this work are expected to provide a minimized size and high density of defects in the YBCO films. In addition, as the BZO nanoparticles are already formed (that is, before their incorporation into the YBCO system), non-coherent interfaces could be generated during the growth of the epitaxial YBCO phase in the films, which may reduce vortice mobility.[35] The influence

of the BZO content on the physicochemical characteristics of the YBCO/BZO *hybrid solutions*, as well as on the morphology and microstructure of the resulting nanocomposite films, is also investigated in this work. Functionality of the YBCO films is demonstrated by their superconducting properties, thus showing the potential of the solution method proposed here for the low-cost fabrication of high-performance coated conductors in long lengths.

Experimental

Synthesis of YBCO/BZO hybrid solutions

A scheme showing the preparation of the precursor solutions of this work is depicted in Figure 2. The BZO nanoparticle dispersion was obtained by a stoichiometric sol-gel reaction of a hydrolytically highly reactive bimetallic alkoxide within nanoscaled reverse micelles.[40,41] It basically consists in the controlled coprecipitation of mono-dispersed and nano-sized amorphous $BaZrO_3$ powder particles by hydrolysis of an heterometallic alkoxide solution through the addition of a water-in-oil (w/o) microemulsion. The composition of the microemulsion was 12.21 wt% 1-pentanol, 3.74 wt% cetyltrimethylammonium bromide (CTAB) cationic surfactant, 11.23 wt% ultrapure degassed and Ar saturated water and 72.82 wt% cyclohexane. After the preparation of the metalloorganic double alkoxide of Ba-Zr by dissolving barium metal in methanol and adding zirconium tetra-n-butoxide to the reaction mixture, a stoichiometric amount of the microemulsion was added dropwise at room temperature. After dilution with anhydrous methyl alcohol (Sigma-Aldrich, 99.8 %), a micelle-stabilized BZO nanoparticle dispersion with a concentration of 5 wt% corresponding to 0.17 M is obtained. On the

other hand, the preparation of the YBCO precursor solution was carried out by dissolution of the respective metallo-organic salts (trifluoroacetates, TFA) in anhydrous methyl alcohol as described elsewhere.[42,43] The concentration of this stoichiometric solution, leading to a $YBa_2Cu_3O_7$ nominal composition, was adjusted to 0.15 M concerning the formula unit. Mixing of the TFA-based YBCO solution and BZO nanoparticle dispersion in various ratios led to the YBCO/BZO hybrid solutions presented here, with molar contents of BZO ranging from 5 to 40 %.

Preparation of YBCO/BZO nanocomposite films

Films from the former hybrid solutions were deposited on 10 mm x 10 mm (100)$LaAlO_3$ single-crystal substrates (CrysTec GmbH, Berlin, Germany) by spin-coating (4000 rpm for 30 s). As-deposited films were pyrolyzed in a moist O_2 atmosphere following different heating ramps up to a final temperature of 400 ºC (total time of the pyrolysis step ~4 h). For crystallization and growth the pyrolyzed films were subsequently heated up to 775 ºC in moist N_2 atmosphere mixed with 100 ppm O_2 gas, maintained for 70 min. The superconducting YBCO phase was obtained after a final treatment at 450 ºC for 120 min under dry O_2 atmosphere. The whole process was carried out in a tube furnace using a gas flux of ~1 L/min.

Materials characterization

The particle size distributions of precursor solutions were determined by dynamic light scattering (DLS) with a Zetasizer Nano particle Analyser (Malvern Instruments Ltd.,

Worcestershire, U.K.). Measurements were carried out using an He-Ne laser at a wavelength of 633 nm and a power of 4 mW. Temperature of the analysis was 25±0.1 °C.

Phase purity and structure of the crystalline films was monitored by X-ray diffraction (XRD) using conventional Bragg–Brentano (θ/2θ) geometry. Measurements were performed in a Philips X-Pert diffractometer (Eindhoven, the Netherlands) with a Cu anode (λ_{Cu} = 1.54 Å). A Zeiss DSM 982 Gemini instrument (Oberkochen, Germany) was used to observe the surface morphology and microstructure of the films by scanning electron microscopy (SEM). Conventional transmission electron microscopy (TEM) imaging, energy-filtered TEM imaging (EFTEM) and electron diffraction was performed on a Zeiss 912 Omega transmission electron microscope provided with an in-column energy filter and operated at 120 kV. High-angle annular dark-field scanning transmission electron microscopy (HAADF)-STEM images were obtained on the aberration-corrected FEI TITAN 'QU-Ant-EM' 80-300 transmission electron microscope operated at 300 kV with a spatial resolution of 0.08 nm in STEM mode. Geometrical phase analysis (GPA) was done using a plugin for DigitalMicrograph.[44,45] TEM sample preparation was done with conventional grinding and polishing followed by argon ion milling. The composition of the films was analyzed by Rutherford backscattering spectroscopy (RBS). Experimental equipment involved a Tandetron Surface Analyzer accelerator with a He^+ beam (1.4 MeV and 1nA). The backscattered ions were collected with a PIXE (Particle Induced X-Ray Emission) detector set at random angle (7º off normal). The RBS experimental data were analyzed using the RUMP simulation program.[46] Error in the calculation of the composition was about 3%.

Current densities of the films were determined resistively via four-point measurements and inductively at 77 K in a Cryoscan System marketed by ThevaDünnschichttechnik GmbH.[47]

Results and discussion

In the current study, the introduction of BZO nanodots into the YBCO system has been carried out by a new approach that involves the mixture of two chemically different solutions, namely, a TFA-based YBCO precursor and a reverse micelle stabilized BZO nanoparticle dispersion. The stability of the resulting hybrid solutions is therefore compromised by the chemical compatibility among the several compounds present in the medium. Homogeneity of both the YBCO precursor solution and the BZO nanoparticle dispersion is denoted by the single and uniform distributions of particle sizes obtained by DLS (Figure 3a and 3b, respectively). An average particle size around 300 nm is deduced from the former one, which must be understood as the size of the molecular building blocks (Y-, Ba-, and Cu-trifluoroacetates) constituent of this solution.[48] In the case of the BZO dispersion, "real" particles (suspended $BaZrO_3$ nanopowders) with a mean size of ~12 nm are detected. This size is intimately related to the diameter of the micelles formed by the microemulsion technique,[49] which allows obtaining very fine and mono-dispersed nanoparticles. These nanoparticle characteristics remains once incorporated into the TFA-based YBCO precursor to form a YBCO/BZO hybrid solution with 10 mol% of BZO content. The respective particle size distribution (Figure 3c) shows two distinctive families of particles that would correspond to the aforementioned oligomeric units of the YBCO precursor, and the BZO nanoparticles. Since the size of the BZO nanoparticles

(now, ~15 nm) is practically maintained with respect to the single dispersion (Figure 3b), it can be concluded that agglomeration of the $BaZrO_3$ nanopowders in the hybrid solution has not occurred. Neither sub-products arisen from secondary reactions are inferred, denoting the chemical compatibility between both solutions, i.e., the YBCO precursor and the BZO dispersion. These results point to the stability of the YBCO/BZO hybrid solutions prepared, even extending up to an aging time of two months (see dash line of Figure 3c). Since the physicochemical features of the BZO nanoparticles are furthermore preserved, the proposed method would be in principle optimum for the CSD preparation of the YBCO/BZO nanocomposite films investigated here.

The development of crystalline phases and epitaxy in the nanocomposite films as a function of the BZO content is shown in the XRD patterns of Figure 4. In all the films the presence of the YBCO phase (JCPDS-ICDD 89-1359) without any trace of impurities is clearly observed (see Fig. 4a). Only diffraction peaks corresponding to (00*l*) planes can be indexed, which proves the epitaxial growth and phase purity of the films. A detailed study in the 2θ range of 37.0-47.0º (see Fig. 4b) denotes the presence of a small peak that may be ascribed to the (200) reflection of the $BaZrO_3$ phase (JCPDS-ICDD 74-1299). Note that its appearance becomes clearer as the concentration of BZO in the films is higher. The much lower intensity of this peak relative to those of the YBCO reflections would be indicative of the randomly-oriented nature of the $BaZrO_3$ phase. As stated in the introduction, artificial defects are mainly formed by addition of secondary phases that grow within the YBCO matrix, that is, during the formation of the epitaxial superconducting phase.[25,28-34,39] This can lead to the heterogeneous nucleation of the secondary phases over the YBCO crystals, thus preserving the epitaxiality in the film. As

example, the formation of two types of BZO nanodots – epitaxial and randomly oriented – were observed in the work of Gutiérrez et al.[34] where the latters are proposed to be mainly responsible for the strong vortex pinning reported. The novelty of the method described here lies in the fact that the BZO nanoparticles introduced into the YBCO system are already formed. Preformed nanoparticles of $BaZrO_3$ are obtained by microemulsion[49] that would promote the generation of non-coherent interfaces during the growth of epitaxial YBCO in the nanocomposite films. Despite the low intensity of the BZO reflections observed by XRD, associated with their apparent absence of preferred orientation, the incorporation of the BZO nanoparticles into the nanocomposite films becomes evident from the direct observation of their surface by SEM (Figure 5). Nanodots corresponding to the BZO nanoparticles are clearly discerned in the microstructure of the films. The increasing amounts of BZO nanoparticle addition (from 5 to 40 mol%) is shown to significantly affect the morphology of the resulting YBCO/BZO nanocomposite films. Thus, smaller amounts lead to isolated BZO nanoparticles (Figure 5 a,b) with grain sizes of ~20 nm which are in the same range than the original grains in the dispersion and compare well with results from literature.[27,30-34] Continuous populations of agglomerates are on the other hand observed in the films with increasing BZO contents from 20 mol% (Figure 5 c-e). To meet the high defect densities demanded today for an effective flux pinning (over 10^{10} cm^{-2}), isolated and randomly-distributed second-phase defects are ideally required in superconducting films. In this work, the nanocomposite films prepared with BZO nanoparticle additions of 5 and 10 mol% would fulfill the aforementioned characteristics. Due to the higher density of BZO nanodots observed in this last film (Figure 5b), the following results of the YBCO/BZO

nanocomposite films will be stressed for the 10 mol% BZO concentration. The cross-section image of this film, shown in Figure 5f, confirms that the distribution of BZO nanoparticles also encompasses the bulk of the layer. Most of these nanoparticles remain isolated, although some aggregates can be observed in both planar and cross-section views. Figure 6 shows further structural and microstructural characterization of the 10 mol% BZO/YBCO nanocomposite film carried out by TEM. BZO nanodots can be discerned from the dark-field image (Figure 6a) with a mean size of 10-20 nm (see inset i). The electron diffraction pattern of this film (see inset ii) evidences the non-coherent nature of the BZO nanodots within the YBCO matrix, where the ring pattern of their diffracted intensities denotes a random distribution of their orientation. Electron spectroscopy imaging confirms the elemental composition of the BZO nanodots (Figure 6b) as deduced from the respective spectra of the Zr $N_{2,3}$ and Ba $N_{4,5}$ edges. A more detailed analysis in this film by HAADF-STEM is shown in Figure 7 a,b, where YBCO (100) planes are shown together with non-coherent BZO nanoparticles of 10-20 nm size in the bulk of the layer (Figure 7a). A sharp interface to the $LaAlO_3$ substrate is also observed, with interfacial semi-coherent BZO nanodots found (Figure 7b). The black arrows indicate Y-248 intergrowths in the YBCO matrix.[50] A geometrical phase analysis on a nanodot revealed a network of edge dislocations denoted as 1 to 8 in Figure 7c. Dumbbell-shaped strain-fields of edge dislocations were directly imaged and the local nanostrain was measured (Figure 7d,e). The regions corresponding to the intergrowths revealed locally highly-strained lattice areas.[48,49]

Figure 8 shows the experimental and simulated spectra obtained by RBS on the YBCO film doped with 10 mol% BZO nanoparticles. Results of the compositional analysis

derived from the simulated curve are summarized in the adjacent table. The number of atoms calculated with regard to the $YBa_2Cu_3O_{7-\delta}$ formula denotes an excellent stoichiometry in the sample. The detection of Zr atoms with an elemental concentration of ~12 % would also account for the presence of $BaZrO_3$ nanoparticles in the film with a content quite close to the expected one (10 mol%). The calculated thickness of the film, consisting of a single layer, resulted in ~130 nm. The relative high fuzzing factor used in the analysis (see table) can be associated with the presence of roughness and maybe porosity in the CSD-derived sample, which might lead to a slight reduction of the superconducting properties. Finally, the critical properties of the YBCO/BZO nanocomposite films on $LaAlO_3$ substrates were analyzed by inductive and resistive measurements. Table 1 presents the results of the inductively measured critical current densities (77 K, 0 T) and the resistively measured main properties of two selected samples. With exception of the film with the highest BZO content (40 mol% BZO) all films show superconductivity, i.e. transition temperatures above liquid nitrogen temperature. With increasing BZO content the inductively determined critical current density ($J_{c,ind}$) decreases, which at first sight seems to indicate that the BZO nanoparticles do not contribute to flux pinning. It is worth mentioning that the presence of agglomerates caused by nanoparticle aggregation may also have an adverse effect on the pinning properties of the films. Subsequently, two films of pure YBCO and YBCO doped with 10 mol% BZO nanoparticles were characterized in more detail by resistive four-point measurements. The temperature dependence of these data are displayed in Figure 9, with the resulting parameters given in the right part of Table 1. In contrast to the inductively determined current density, the resistive measurement shows a clear

improvement of the characteristic and critical properties of the superconducting film with BZO nanoparticles. The transition temperature T_c is slightly enhanced, with transition width ΔT_c notably lowered, the specific resistance ρ(100 K) is reduced, the resistance ratio R(300 K)/R(100 K) is increased, and last but not least the critical current $J_{c,res}$ (77 K,0 T) is significantly improved by a factor of three. Nevertheless, the absolute value of $J_{c,res}$ is much smaller than the $J_{c,ind}$ one for both samples. This discrepancy can be explained by the difference in the measuring principle and it provides a deeper insight into the impact of the BZO nanoparticles on the morphology of the sample.

In general, inductive measurements of the critical properties of a superconductor are based on the Bean critical state model. The inductive signal records the screen current of the superconducting sample. If the geometrical arrangement of the setup and the sample size are identical, a change of the inductive signal is caused by a change of the critical current of the sample or by a rearrangement of the shielding current. For a perfect homogeneous superconductor a rearrangement of the shielding current is not expected, therefore the inductive signal is directly related to the critical current. However, for an inhomogeneous superconductor the signal is composed of all shielding currents detected by the sensor coil. For instance, for a granular superconducting film the overall shielding of the film (including intergranular currents) as well as the contributions of the individual grains (intragranular currents) have to be taken into account. A modification of the interconnectivity of the individual grains would lead to a modification of the 'path' of the shielding current. Typically, an improvement of the grain boundary (i.e. improvement of the intergranular critical current) results in an increase of the shielded area and therefore to a reduction of the inductive signal even if the critical properties of the grains

(intragranular critical current) are unaltered. Our experimental setup is calibrated for homogeneous superconductors. Therefore, the reduction of $J_{c,ind}$ with BZO content can be indicative of an improvement in the homogeneity of the sample, i.e. improvement of the intergranular current. In contrast, the resistive measurements provide the 'real' critical current between the voltage contacts. In case of a granular superconductor the critical current will be dominated by the lowest value on a percolative path between the contacts which is the intergranular critical current. Our measurements therefore indicate that the chemically deposited films of this work display inhomogeneous critical properties (most likely they are granular). The inductive measurements revealed that the critical properties of the YBCO grains (intragranular critical current) are comparable to those of perfect epitaxial films. As explained, the intragranular properties lead however to a strong reduction of the overall critical current determined by resistive measurements. This shortcoming can be cured by the BZO nanoparticles. The addition of BZO nanoparticles results in a significant improvement of the interconnectivity among grains and consequently the intergranular current is strongly enhanced. Already by adding 10 mol% of BZO, the overall critical current approaches values that are comparable to literature ones. We can therefore state that, although we cannot demonstrate that the BZO nanodots behave as artificial pinning centers in the superconducting matrix (if they do the effect is small), they seem to improve the homogeneity of the superconducting film leading to a significant increase of the resistively measured (hence technically relevant) critical current density. In this way, the superconducting properties shown of the YBCO/BZO nanocomposite films support their functionality as 2G HTS wires, or coated conductors, and demonstrate the reliability of the fabrication method presented here.

Conclusions

Superconducting $YBa_2Cu_3O_{7-\delta}$ (YBCO) films with embedded $BaZrO_3$ (BZO) nanodots can be successfully prepared by a low-cost chemical solution deposition (CSD) method involving hybrid solutions comprised of TFA-based YBCO precursors and reverse micelle stabilized BZO nanoparticle dispersions. This novel approach represents a significant innovation over previous techniques in which the growth of second-phase defects is developed together with the formation of the epitaxial superconducting phase. Here, the preparation of the BZO nanoparticles is carried out by microemulsion-mediated synthesis, allowing the formation of nano-sized and mono-dispersed particles that preserve their features once introduced into the TFA-based YBCO solution. A high density of isolated second-phase defects consisting in BZO nanodots is achieved over the whole microstructure of the nanocomposite films by tuning the amount of BZO nanoparticles introduced in the system. Two types of local lattice defects are identified and imaged, i.e., misfit edge dislocations and Y-248 intergrowths. The misfit interfacial dislocations at the BZO-YBCO interface have an inter-distance of less than 2 nm. Geometrical phase analysis yields a dumbbell shaped strain-field of these edge dislocations and locally highly-strained lattice areas at the intergrowths. The resistively measured critical current of the YBCO films improves considerably by the presence of such BZO nanodots, which has been rather ascribed to an improved morphology of the sample (i.e. improved intergranular critical current density) than to improvement of the flux pinning provided by the BZO nanodots. This interpretation is supported by the combination of inductive and resistive measurements of the critical properties. The

flexibility of the solution method presented, by which the nanoparticle synthesis can be potentially transferred to any other oxide system, opens up a wealth of possibilities in the design and investigation of coated conductors based on nanostructured films with new (and rare) artificial second-phase defects.

Acknowledgements

This work was supported by the German Federal Ministry of Economics and Technology (BMWi) contract no. 0327433A (project ELSA). L. Molina-Luna and G. Van Tendeloo acknowledge funding from the European Research Council (ERC grant no. 24691-COUNTATOMS). The authors gratefully acknowledge J. Dornseiffer for the support with preparation of the microemulsions for the BZO nanoparticles; G. Wasse for the SEM images; and T. Pössinger for the preparation of the artwork.

References

(1) A. V. Narlikar, *High Temperature Superconductivity*, Springer-Verlag, Berlin, 2004.

(2) D. P. Norton, A. Goyal, J. D. Budai, D. K. Christen, D. M. Kroeger, E. D. Specht, Q. He, B. Saffian, M. Paranthaman, C. E. Klabunde, D. F. Lee, B. C. Sales and F. A. List, *Science*, 1996, **274**, 755.

(3) D. Larbalestier, A. Gurevich, D. M. Feldmannand and A. Polyanskii, *Nature*, 2001, **414**, 368.

(4) V. Selvamanickam, Y. Chen, X. Xiong, Y. Y. Xie, J. L. Reeves, X. Zhang, Y. Qiao, K. P. Lenseth, R. M. Schmidt, A. Rar, D. W. Hazelton and K. Tekletsadik, *IEEE Trans. Appl. Supercond.*, 2007, **17**, 3231.

(5) M. P. Paranthaman and T. Izumi, *MRS Bull.*, 2004, **29**, 533.

(6) A. P. Malozemoff, J. Mannhart and D. Scalapino, *Phys. Today*, 2005, **4**, 41.

(7) W. V. Hassenzahl, D. W. Hazelton, B. K. Johnson, P. Komarek, M. Noe and C. T. Reis, *Proc. IEEE*, 2004, **92**, 1655.

(8) A. Goyal, *Second Generation HTS Conductors*, Kluwer Academic, Netherlands, 2004.

(9) T. Schneller, R. Waser, M. Kosec and D. Payne, *Chemical Solution Deposition of Functional Oxide Thin Films*, Springer, Wien, 2013.

(10) M. Bäcker, M. Falter, O. Brunkahl and B. Holzapfel, "Superconducting Films", in: T. Schneller, R. Waser, M. Kosec and D. Payne, *Chemical Solution Deposition of Functional Oxide Thin Films*, Springer, Wien, 2013.

(11) J. Feys, P. Vermeir, P. Lommens, S. C. Hopkins, X. Granados, B. A. Glowacki, M. Baecker, E. Reich, S. Ricard, B. Holzapfel, P. Van der Voort and I. Van Driessche, *J. Mater. Chem.*, 2012, **22**, 3717.

(12) M. P. Paranthaman, S. Sathyamurthy, M. S. Bhuiyan, P. M. Martin, T. Aytug, K. Kim, M. Fayek, K. J. Leonard, J. Li, A. Goyal, T. Kodenkandath, X. Li, W. Zhang and M. W. Rupich, *IEEE T. Appl. Supercon.*, 2007, **17**, 3332.

(13) J. Gázquez, F. Sandiumenge, M. Coll, A. Pomar, N. Mestres, T. Puig, X. Obradors, Y. Kihn, M. J. Casanove and C. Ballesteros, *Chem. Mater.*, 2006, **18**, 6211.

(14) S. Engel, K. Knoth, R. Hühne, R. Schultz and B. Holzapfel, *Supercond. Sci. Technol.*, 2005, **18**, 1385.

(15) M. W. Rupich, D. T. Verebelyi, W. Zhang, T. Kodenkandath and X. Li, *MRS Bull.*, 2004, **29**, 572.

(16) R. W. Schwartz , *Chem. Mater.*, 1997, **9**, 2325.

(17) B. A. Albiss and I. M. Obaidat, *J. Mater. Chem.*, 2010, **20**, 1836.

(18) X. Obradors, T. Puig, A. Pomar, F. Sandiumenge, N. Mestres, M. Coll, A. Cavallaro, N. Romà, J. Gázquez, J. C. González, O. Castaño, J. Gutiérrez, A. Palau, K. Zalamova, S. Morlens, A. Hassini, M. Gibert, S. Ricart, J. M. Moretó, S. Piñol, D. Isfort and J. Bock, *Supercond. Sci. Technol.*, 2006, **19**, S13.

(19) M. P. Siegal, P. G. Clem, J. T. Dawley, R. J. Ong, M. A. Rodriguez and D. L. Overmyer, *Appl. Phys. Lett.*, 2002, **80**, 2710.

(20) A. Llordés, K. Zalamova, S. Ricart, A. Palau, A. Pomar, T. Puig, A. Hardy, M. K. Van Bael and X. Obradors, *Chem. Mater.*, 2010, **22**, 1686.

(21) C. Gerber, D. Anselmetti, J. G. Bednorz, J. Mannhart and D. G. Schlom, *Nature*, 1991, **350**, 279.

(22) K. Matsumoto and P. Mele, *Supercond. Sci. Technol.*, 2010, **23**, 014001.

(23) J. M. Huijbregtse, B. Dam, R. C. F. van der Geest, F. C. Klaassen, R. Elberse, J. H. Rector and R. Griessen, *Phys. Rev. B*, 2000, **62**, 1338.

(24) B. Dam, J. M. Huijbregtse, F. C. Klaassen, R. C. F. van der Geest, G. Doornbos, J. H. Rector, A. M. Testa, S. Freisem, J. C. Martinez, B. Stäuble-Pümpin and R. Griessen, *Nature*, 1999, **399**, 439.

(25) T. G. Holesinger, L. Civale, B. Maiorov, D. M. Feldmann, J. Y. Coulter, D. J. Miller, V. A. Maroni, Z. Chen, D. C. Larbalestier, R. Feenstra, X. Li, Y. Huang, T. Kodenkandath, W. Zhang, M. W. Rupich and A. P. Malozemoff, *Adv. Mater.*, 2008, **20**, 391.

(26) L. Civale, A. D. Marwick, T. K. Worthington, M. A. Kirk, J. R. Thompson, L. Krusin-Elbaum, Y. Sun, J. R. Clem and F. Holtzberg, *Phys. Rev. Lett.*, 1991, **67**, 648.

(27) T. Haugan, P. N. Barnes, R. Wheeler, F. Meisenkothen and M. Sumption, *Nature*, 2004, **430**, 867.

(28) A. A. Gapud, R. Feenstra, D. K. Christen, J. R. Thompson and T. G. Holesinger, *IEEE Trans. Appl. Supercond.*, 2005, **15**, 2578.

(29) Y. Yamada, K. Takahashi, H. Kobayashi, M. Konishi, T. Watanabe, A. Ibi, T. Muroga, S. Miyata, T. Kato, T. Hirayama and Y. Shiohara, *Appl. Phys. Lett.*, 2005, **87**, 132502.

(30) N. Long, N. Strickland, B. Chapman, N. Ross, J. Xia, X. Li, W. Zhang, T. Kodenkandath, Y. Huang and M. Rupich, *Supercond. Sci. Technol.*, 2005, **18**, S405.

(31) J. L. Macmanus-Driscoll, S. R. Foltyn, Q. X. Jia, H. Wang, A. Serquis, L. Civale, B. Maiorov, M. E. Hawley, M. P. Maley and D. E. Peterson, *Nature Mater.*, 2004, **3**, 439.

(32) J. Hänisch, C. Cai, R. Hühne, L. Schultz and B. Holzapfel, *Appl. Phys. Lett.*, 2005, **86**, 122508.

(33) A. Goyal, S. Kang, K. J. Leonard, P. M. Martin, A. A. Gapud, M. Varela, M. Paranthaman, A. O. Ijaduola, E. D. Specht, J. R. Thompson, D. K. Christen, S. J. Pennycook and F. A. List, *Supercond. Sci. Technol.*, 2005, **18**, 1533.

(34) J. Gutiérrez, A. Llordes, J. Gázquez, M. Gibert, N. Romà, S. Ricart, A. Pomar, F. Sandiumenge, N. Mestres, T. Puig and X. Obradors, *Nature Mater.*, 2007, **6**, 367.

(35) E. Bartolomé, A. Palau, A. Llordes, T. Puig and X. Obradors, *Phys. Rev. B*, 2010, **81**, 184530.

(36) K. J. Leonard, S. Sathyamurthy and P. Paranthaman, *Chem. Mater.*, 2005, **17**, 4010.

(37) H. Herrig and R. Hempelmann, *Mater. Lett.*, 1996, **27**, 287.

(38) L. Civale, B. Maiorov, A. Serquis, J. O. Willis, J. Y. Coulter, H. Wang, Q. Jia, P. N. Arendt, J. L. MacManus-Driscoll, M. P. Maley and S. R. Foltyn, *Appl. Phys. Lett.*, 2004, **84**, 2121.

(39) P. Mele, K. Matsumoto, T. Horide, O. Miura, A. Ichinose, M. Mukaida, Y. Yoshida and S. Horii, *Supercond. Sci. Technol.*, 2006, **19**, 44.

(40) C. Pithan, T. Schneller, Y. Shiratori, S. B. Majumber, F.-H. Haegel, J. Dornseiffer and R. Waser, *J. Int. J. Mat. Res.*, 2006, **97**, 5.

(41) T. Schneller, S. Halder, R. Waser, C. Pithan, J. Dornseiffer, Y. Shiratori, L. Houben, N. Vyshnavi and S. B. Majumder, *J. Mater. Chem.*, 2011, **21**, 7953.

(42) A. Gupta, R. Jagannathan, E. I. Cooper, E. A. Giess, J. I. Landman and B. W. Hussey, *Appl. Phys. Lett.*, 1988, **52**, 2077.

(43) I. V. Driessche, J. Feys, S. C. Hopkins, P. Lommens, X. Granados, B. Glowacki, S. Ricart, B. Holzapfel, M. Vilardell, A. Kirchner and Baecker, *Supercond. Sci. Technol.*, 2012, **25**, 065017.

(44) M. J. Hytch, E. Snoeck and R. Kilaas, *Ultramicroscopy*, 1998, **74**, 131.

(45) M. J. Hytch, J-L. Putaux, and J-M. Penisson, *Nature*, 2003, **423**, 270.

(46) M. Mayer, *S.I.M.R.A. User's Guide*. Technical Report IPP 9/113, Max Planck Institut für Plasmaphysic, Garching (2006).

(47) See http://www.theva.com/prod/cryoscan. Accessed September 04, 2014.

(48) C. Sanchez, G. J. de A. A. Soler-Illia, F. Ribot, T. Lalot, C. R. Mayer and V. Cabuil, *Chem. Mater.*, 2001, **13**, 3061.

(49) C. Pithan, Y. Shiratori, R. Waser, J. Dornseiffer and F.-H. Haegel, *J. Am. Ceram. Soc.*, 2006, **89**, 2908.

(50) A. Llordés, A. Palau, J. Gázquez, M. Coll, R. Vlad, A. Pomar, J. Arbiol, R. Guzmán, S. Ye, V. Rouco, F. Sandiumenge, S. Ricart, T. Puig, M. Varela, D. Chateigner, J. Vanacken, J. Gutiérrez, V. Moshchalkov, G. Deutscher, C. Magen and X. Obradors, *Nat. Mater.*, 2012, **11**, 329.

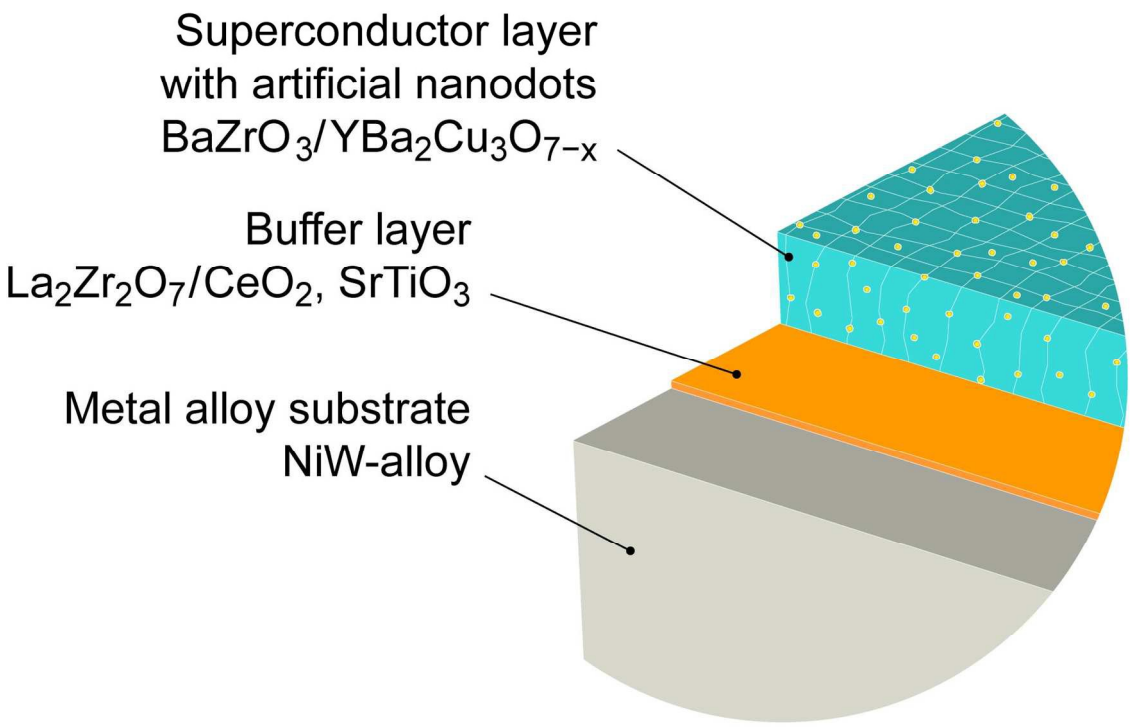

Figure 1. Typical layer architecture of a coated conductor prepared by chemical solution deposition.

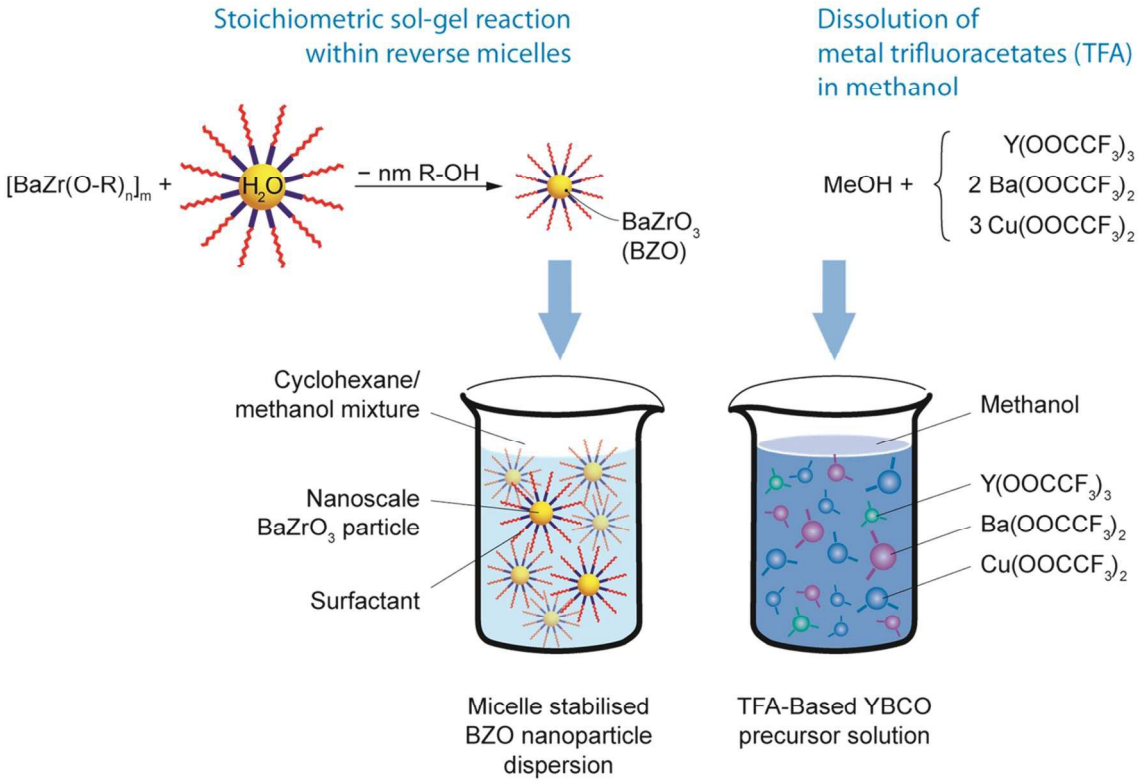

Figure 2. Scheme, showing the preparation of the precursor solutions of this work. Hybrid solutions result from the mixture between the TFA-based YBCO precursor and the reverse micelle stabilized BZO nanoparticle dispersion in different molar ratios.

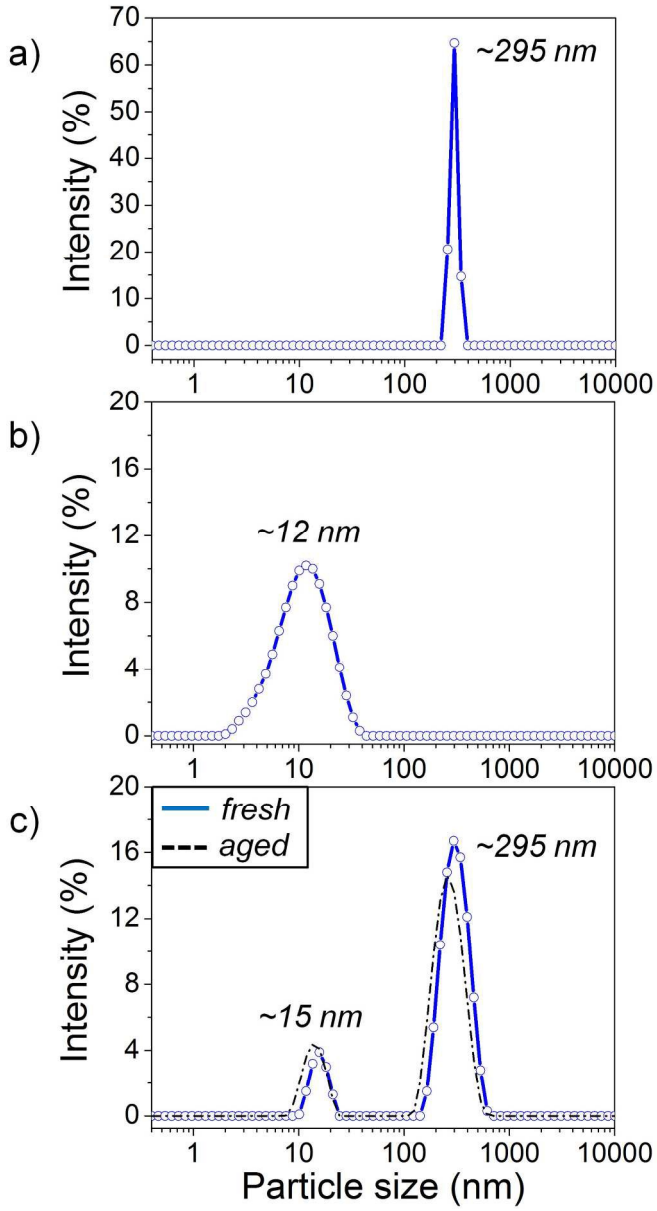

Figure 3. Particle size distributions obtained by DLS of the (a) pure TFA-based YBCO precursor (0.15 M), (b) pure reverse micelle stabilized BZO nanoparticle dispersion (5 wt%), and (c) a YBCO/BZO hybrid solution with 10 mol% of BZO content.

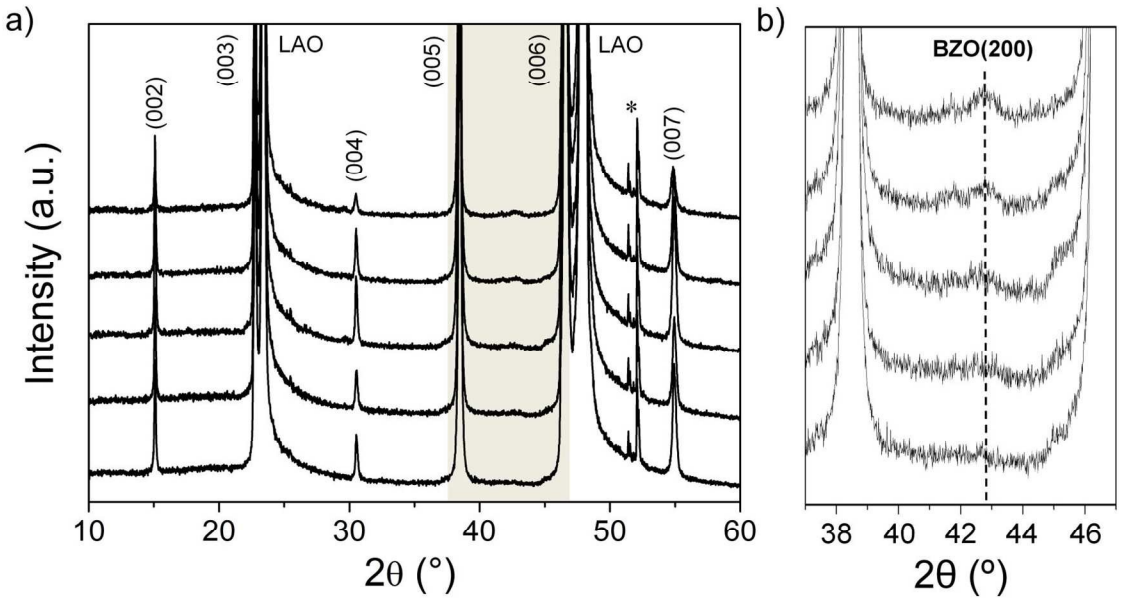

Figure 4. (a) XRD patterns of the YBCO/BZO nanocomposite films with 5 mol%, 10 mol%, 20 mol%, 30 mol%, and 40 mol% of BZO content and (b) magnification in the 37-47 º 2θ range. (LAO = $LaAlO_3$ substrate, * = artefact).

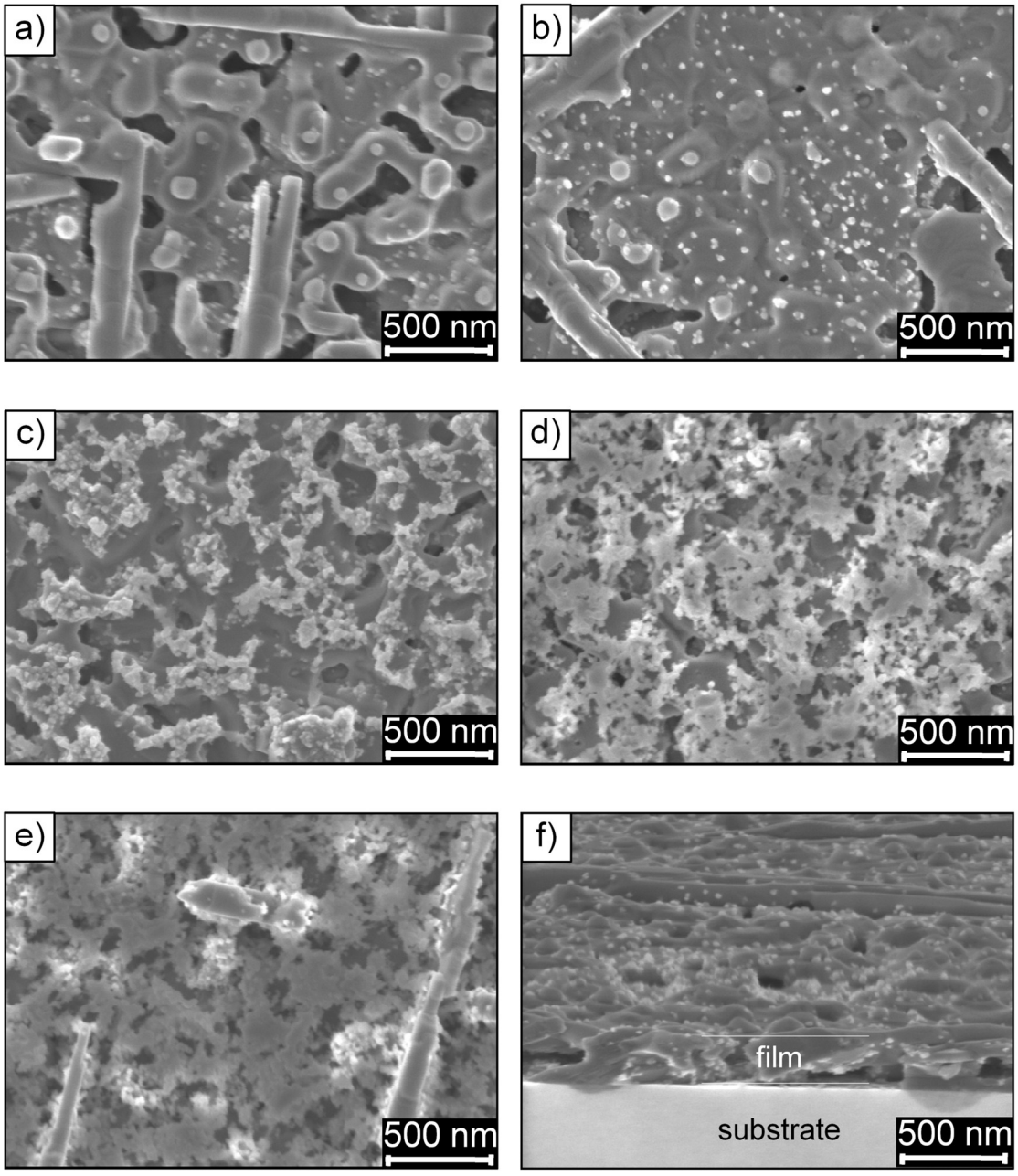

Figure 5. SEM images of the YBCO/BZO nanocomposite films with (a) 5 mol%, (b) 10 mol%, (c) 20 mol%, (d) 30 mol%, and (e) 40 mol% of BZO content. (f) Cross-section image of the 10 mol% BZO/YBCO nanocomposite film.

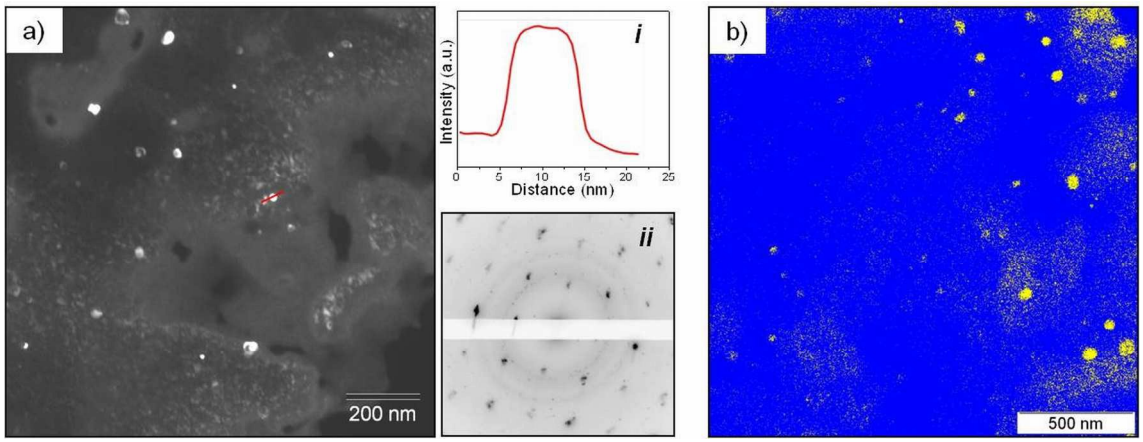

Figure 6. (a) Dark-field TEM image of the 10 mol% BZO/YBCO nanocomposite film. Inset i shows the intensity line scan of a nanodot. Inset ii shows the electron diffraction pattern of the nanocomposite film. (b) Color phase mapping of BZO nanodots in the film.

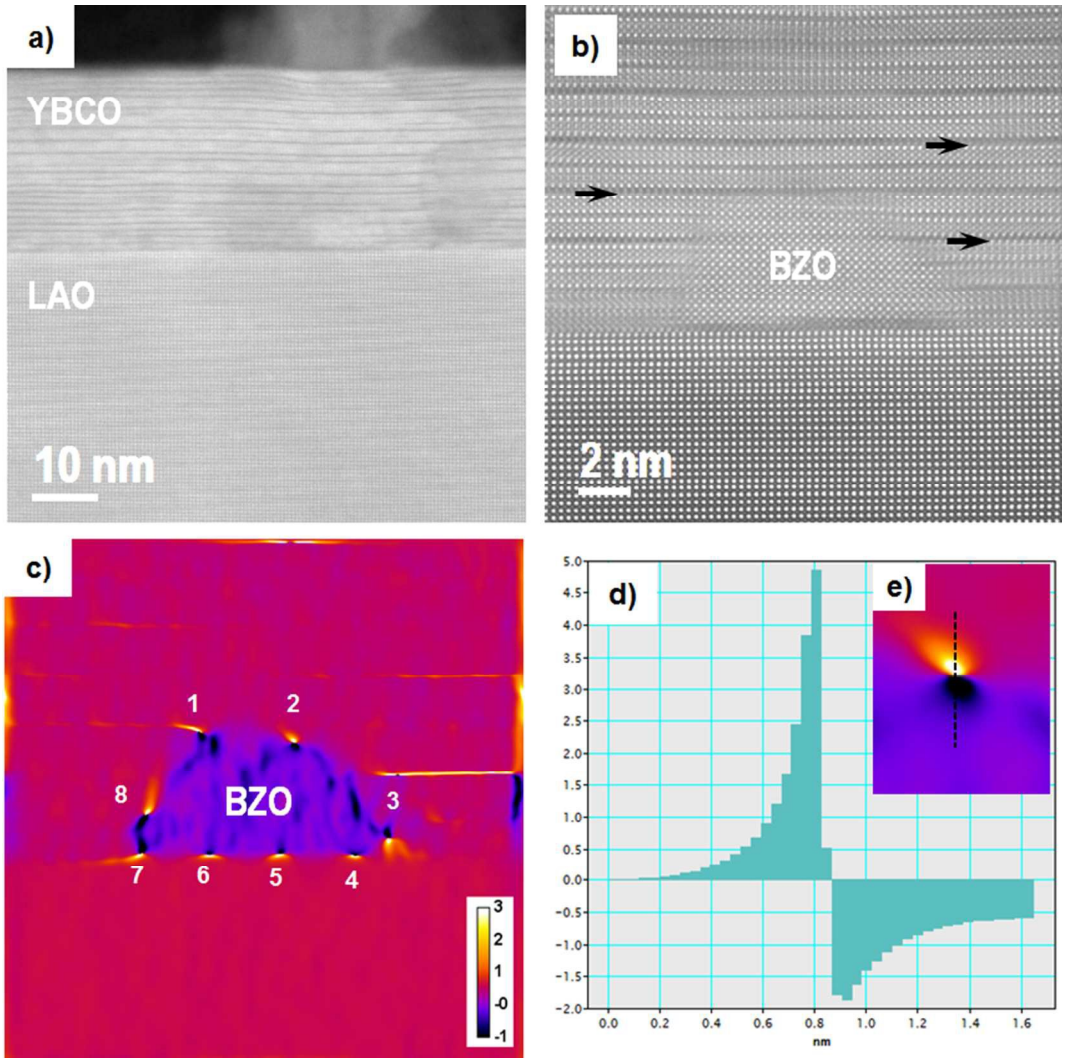

Figure 7. (a) HAADF-STEM image of the 10 mol% BZO/YBCO nanocomposite film in cross-section. YBCO (100) planes are observed. (b) HAADF-STEM image of an interfacial $BaZrO_3$ nanodot. The black arrows indicate Y-248 intergrowths in the YBCO matrix. (c) GPA map visualizing the nanostrain along the in-plane direction corresponding to the ε_{xx} component of the strain matrix. A network of edge dislocations is revealed and denoted as 1 to 8 in the image. The scale bar denotes the strain %. (d) Line-scan along an edge dislocation (2). (e) Dumbbell-shaped strain-field of an edge dislocation (2).

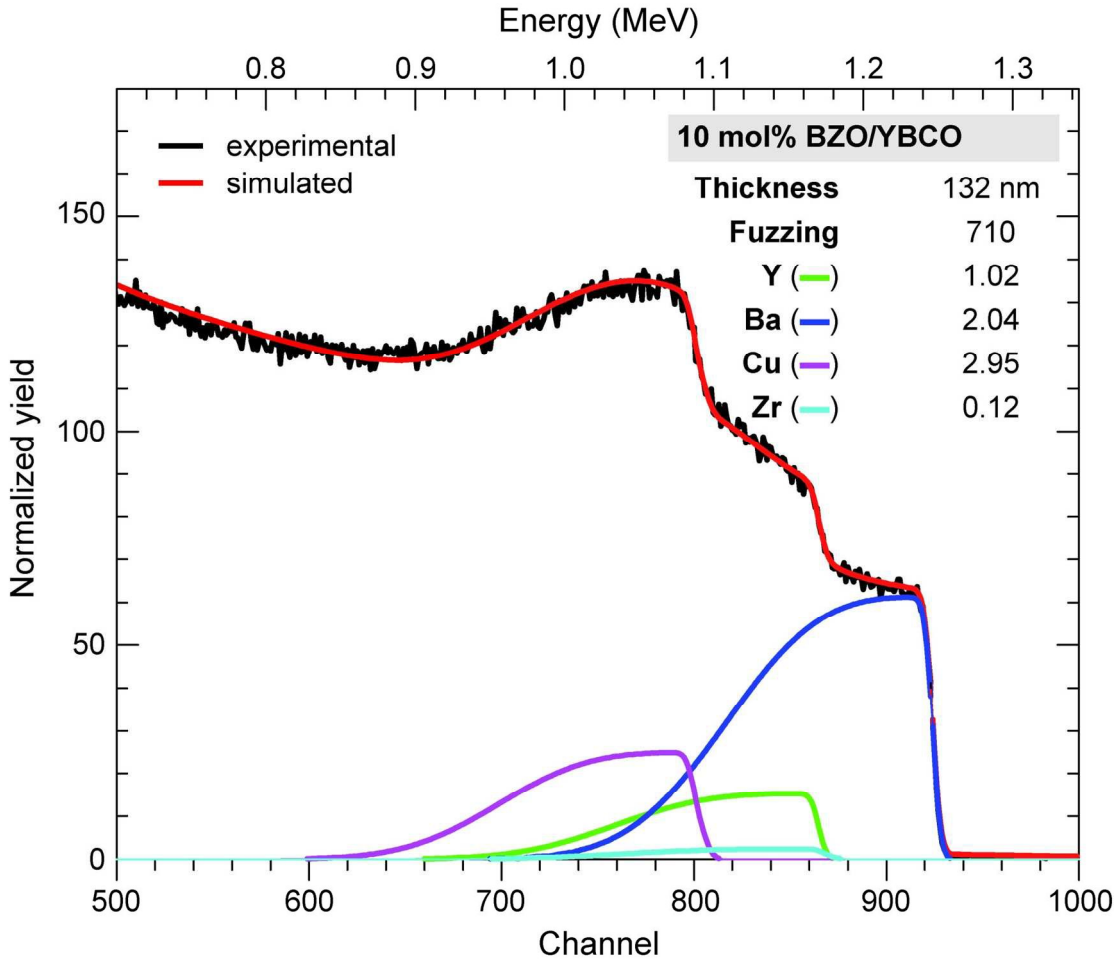

Figure 8. RBS spectra of the YBCO/BZO nanocomposite film with 10 mol% of BZO content. Atomic concentration and other relevant data calculated from the simulated curve are collected in the inset.

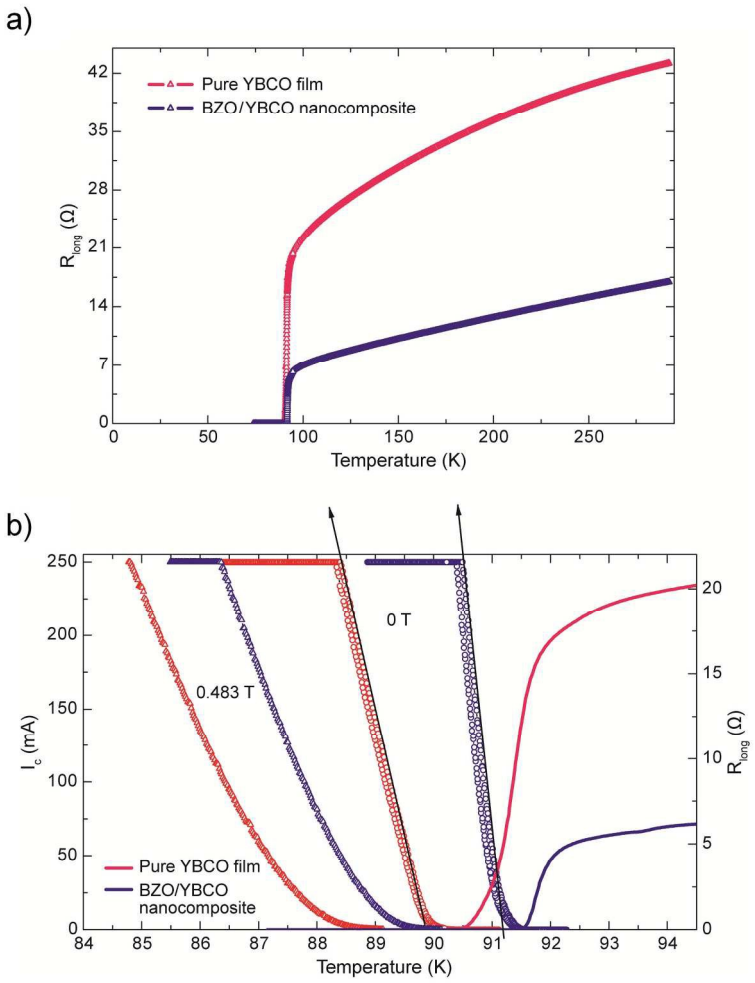

Figure 9. Temperature dependence of the (a) normal state resistance and (b) critical current at 0 and 0.483 T for the pure YBCO and 10 mol% BZO/YBCO nanocomposite films.

Table 1. Summary of the superconducting properties of the films of this work. Comparison between the pure YBCO and 10 mol% BZO/YBCO nanocomposite films is stressed.

	Current density (MA/cm^2)		Pure YBCO	10 mol% BZO/YBCO
Pure YBCO	2.55	**R(300 K)/R(100 K)**	1.95 (non linear)	2.4
5 mol% BZO/YBCO	1.77	**$T_{c,off}$**	90.1 K	91.33 K
10 mol% BZO/YBCO	1.04	**ΔT_c**	0.69 K	0.33 K
20 mol% BZO/YBCO	0.60			
30 mol% BZO/YBCO	0.84	**ρ(100 K)***	6.1 μΩm	1.6 μΩm
40 mol% BZO/YBCO	–	**J_c(77 K)**	0.23 MA/cm^2	0.69 MA/cm^2

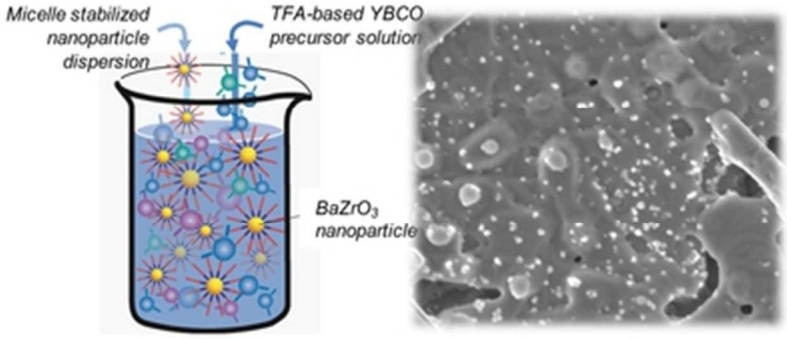

35x14mm (300 x 300 DPI)